Structural and thermal effects of ion-irradiation induced defect configurations in silicon

Krishnan Swaminathan-Gopalan,* Taishan Zhu,* Elif Ertekin,† and Kelly A. Stephani‡
Department of Mechanical Science and Engineering
and University of Illinois at Urbana-Champaign, Illinois, USA
(Received 23 January 2017; revised manuscript received 30 March 2017; published 24 May 2017)

Classical molecular dynamics calculations were used to investigate the formation of defects produced during irradiation of energetic ions on silicon. The aim of this study was to characterize the nature of defects and defective regions formed through ion irradiation and to establish a connection between the ion irradiation parameters, lattice defect configurations, and the resulting modified lattice thermal conductivity of silicon. The defective regions were characterized according to the total number of defects generated, the size and the density of the defective region, and the longitudinal and radial distribution of defects along the ion impact path. In addition, the clustering of the defects into amorphous pockets is analyzed and the effect of these processing parameters on the properties of the clusters is also studied. Further, the lattice defect configurations produced during continuous bombardment of multiple ions are directly investigated and compared to the single-ion impact results. A range of irradiation parameters including ion species, ion energies, fluence, and beam width have been explored to elucidate the dependence of the resulting defect configurations on these experimental design parameters. High density defective regions are found to be produced by low-energy ions with high atomic number. Analysis of the defects produced under varying beam diameters indicates that the beam diameter, rather than the beam energy, is the more prominent factor in determining the extent of the defective region. We demonstrate that the thermal conductivity of the material is most significantly influenced by the effective diameter of the defective region, making the beam diameter the most influential experimental parameter for tuning the lattice thermal conductivity. A reduction in thermal conductivity of up to 80% from pristine silicon was achieved with the processing parameters used in this work. This study indicates that ion beam irradiation can be a realizable manufacturing process with high tunability and control to achieve desired material properties.

DOI: 10.1103/PhysRevB.95.184109

I. INTRODUCTION

Defects in a crystal lattice, either in the form of vacancies or impurities, lead to modification of the intrinsic crystal properties and are usually undesirable. However, in some cases, introducing strategic lattice defects may have an overall beneficial effect on the properties of the system. Doping semiconductors by ion implantation is one of the most common examples [1]. Another important application is the use of defects to enhance the efficiency of thermoelectric devices [2–4]. Some of the other benefits include tailoring of mechanical, electrical, and magnetic properties of nanostructured materials [5–7], fabrication of nanodots, clusters, self-organization and assemblies, etc. [8].

Ion beam irradiation is one of the most popular methods for strategic material processing since it offers a range of experimental parameters to selectively introduce defects into the lattice [8]. Optimal defect configurations can be produced by modifying the design parameters such as ion species, energy, incidence angle, fluence, etc. However, a precise knowledge of the type, abundance, and configuration of the defects formed due to the irradiation process is essential, in order to achieve desirable properties. Earlier computational models used the binary collision approximation (BCA), which is useful for understanding the transport of ions in the target. However, the BCA does not account for the secondary and overlapping collision cascades, and is therefore not suited for examining the defect formation in the lattice and the resultant modification in the material properties. Simulations using classical molecular dynamics (MD) can provide detailed information regarding the interactions of the atoms and thereby capture the evolution of collision cascades and generation of lattice defect configurations.

Although there is a wide literature of MD simulations of ion-beam irradiation [9–15], most of these studies have focused on the evolution of collision cascades on a defect-free lattice. However, in most scenarios, the ion-irradiation cascades are produced from a continuous beam source, involving repeated bombardment of the lattice which alters the subsequent collision cascade details. In this study, MD simulations are employed to gain quantitative information on the creation of defect configurations in three-dimensional silicon lattice under continuous ion bombardment in a tight ion beam setup such as those used in focused ion beam (FIB) processing. A wide range of design parameters including ion species, ion energies, fluence, and beam width have been explored to understand the variations in the defect configuration. This study also analyzes the change in the thermal properties of the material due to the ion beam irradiation. These data can be utilized to select the suitable irradiation parameters to introduce specific types of defects in a Si target for tailoring the desired material properties. The utility of this information in computing the figure of merit for thermoelectric materials is demonstrated in Ref. [16].

*Ph.D. candidate, Department of Mechanical Science and Engineering.
†Assistant Professor, Department of Mechanical Science and Engineering.
‡Assistant Professor, Department of Mechanical Science and Engineering; Corresponding author: ksteph@illinois.edu

This paper is organized as follows: the simulation details of the ion-irradiation process are presented in Sec. II. Section III outlines the different methods of characterizing the defect configurations and the structural properties that are adopted in this work. Section IV describes the Green-Kubo formulation, which is employed to calculate the thermal conductivity of the defective systems using equilibrium MD. Analysis of the effect of the design parameters on the defect configuration, and the structural and thermal properties of the system is discussed in Sec. V, followed by conclusions in Sec. VI.

II. SIMULATION METHODOLOGY

The classical MD calculations employed in this study were performed using HOOMD-blue [17], which utilizes Nvidia's CUDA computing architecture and is optimized to run on Graphics Processing Units (GPUs). The interactions between the ions and the silicon atoms are modeled using the Ziegler-Biersack-Littmark (ZBL) universal repulsive potential [18]. The ZBL potential is a purely repulsive potential and takes the form of a screened Coloumbic interaction:

$$V_{ij}^{\mathrm{ZBL}} = \frac{1}{4\pi\epsilon_0}\frac{Z_i Z_j e^2}{r_{ij}}\phi\left(\frac{r_{ij}}{a}\right), \tag{1}$$

where Z_i and Z_j are the atomic numbers of the two atoms, e is the charge of the electron and ϵ_0 is the permittivity of free space. The effective screening length, a is defined as

$$a = \frac{0.8854 a_0}{Z_i^{0.23} + Z_j^{0.23}}, \tag{2}$$

where a_0 is the Bohr radius and ϕ is the universal screening function, which is obtained empirically from a fit to core electron overlap calculations [18] and follows the form

$$\phi(x) = 0.1818\mathrm{e}^{-3.2x} + 0.5099\mathrm{e}^{-0.9423x} + 0.2802\mathrm{e}^{-0.4029x} + 0.02817\mathrm{e}^{-0.2016x}. \tag{3}$$

The Tersoff Si (C) potential [19] is used to model the interactions between the silicon atoms. The Tersoff potential is widely used to model Silicon systems and was chosen since it describes the defect formation energies well. This potential is then smoothly joined to a short-range repulsive potential based on ZBL potential that describes the energetic interactions at short interatomic distances:

$$V_{ij} = (1 - f_F(r_{ij}))V_{ij}^{\mathrm{ZBL}} + f_F(r_{ij})V_{ij}^{\mathrm{Tersoff}}. \tag{4}$$

Here, the f_F term is Fermi-like smoothing function that joins the Tersoff and ZBL potentials:

$$f_F(r_{ij}) = \frac{1}{1 + A_F \exp(r_{ij} - r_C)}. \tag{5}$$

The Tersoff potential is a bond order potential, and thus accounts for factors such as the number of bonded neighbors, bond lengths, bond angles, etc. A bond-order potential can describe the several different bonding stages of an atom and thus, to some extent can describe the bond transformations correctly. It is a three-body potential and has the following form:

$$V_{\mathrm{Tersoff}} = \frac{1}{2}\sum_{i\neq j} f_c(r_{ij})[f_r(r_{ij}) + b_{ij} f_A(r_{ij})], \tag{6}$$

where f_R and f_A are the repulsive and attractive terms respectively, that take the form of a Morse potential:

$$f_R(r) = A\exp(-\lambda_1 r), \quad f_A(r) = B\exp(-\lambda_2 r). \tag{7}$$

The strength of the attractive term is determined by the coefficient b_{ij} called the modifier term, which accounts for the number of bonded neighbors (environment of the atom) and enforces bond angles between the atoms. This is of the form

$$b_{ij} = \left(1 + \beta^n \zeta_{ij}^n\right)^{-\frac{1}{2n}}, \quad \zeta_{ij} = \sum_{k\neq i,j} f_c(r_{ik}) g(\theta_{ijk}) \exp\left(\lambda_3^3 (r_{ij} - r_{ik})^3\right), \tag{8}$$

$$g(\theta_{ijk}) = 1 + \frac{c^2}{d^2} - \frac{c^2}{d^2 + (h - cos\theta_{ijk})^2},$$

where f_c is the cutoff function that limits the range of interaction between the atoms by smoothly transitioning the potential to zero at some finite distance, given by

$$f_c(r) = \begin{cases} 1, & r \leqslant R - D \\ \frac{1}{2} - \frac{1}{2}\sin\left(\frac{\pi}{2}\frac{r-R}{D}\right), & R - D < r < R + D. \\ 0, & r \geqslant R + D. \end{cases} \tag{9}$$

The Tersoff and the Tersoff/ZBL parameters used in this study and their references are presented in Table I. For the energy ranges explored in this study, the inelastic energy losses due to collisions with electrons (electronic stopping) do not lead to atomic displacements, but can become significant in dissipating energy from the incoming ion and secondary recoils. An energy dependent frictional force was employed based on the Ziegler-Biersack-Littmark model [20] to capture energy transfer due to electronic stopping. This energy is simply removed from the ion and atoms, and does not contribute to damage production in the target [21]. The term "ion" is used only to provide a direct context to the experimental setup and the charge of the atom is not explicitly considered. This is justified within the Born-Oppenheimer approximation since the charge of the ion would be neutralized on the surface by Auger neutralization [22], considering that the electron movement is at least three orders of magnitude faster than the nuclei [23].

The side view of a representative 3D simulation domain is shown in Fig. 1. The top surface is exposed to vacuum, and one layer of atoms at the bottom are fixed to prevent the

TABLE I. Tersoff [24] and Tersoff/ZBL [25] potential parameters used in molecular dynamics simulations.

Parameter	Value	Parameter	Value
A (eV)	1830.8	β	1.0999×10^{-6}
B (eV)	471.18	n	0.78734
λ_1 (Å^{-1})	2.4799	c	1.0039×10^5
λ_2 (Å^{-1})	1.7322	d	16.218
λ_3 (Å^{-1})	1.7322	h	−0.59826
R (Å)	2.85	A_F	14
D (Å)	0.15	r_C	0.95

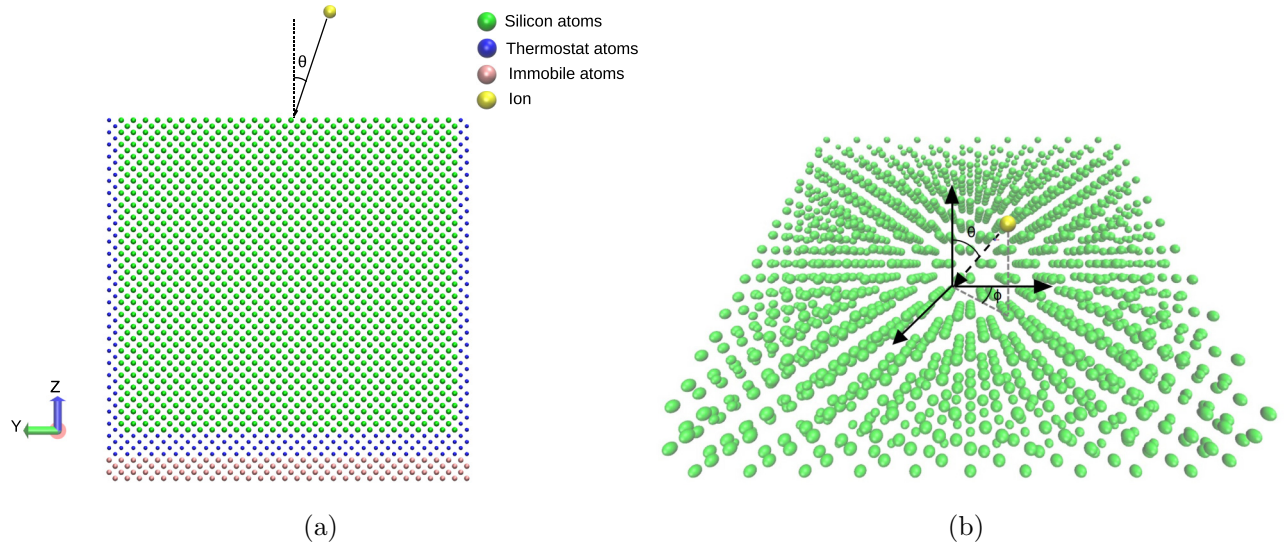

FIG. 1. Schematic illustration of (a) side view and (b) perspective top view of the 3D simulation setup. Silicon atoms at the bottom are fixed. Thermostat atoms are present at the bottom and at the four sides. Ions are introduced above the lattice at the specified polar angle θ and azimuthal angle ϕ relative to the basal plane surface normal.

lattice from translating. Thermostat atoms are applied to a layer of atoms at the bottom and on the four sides of the sample. This models the dissipation of energy to the surrounding lattice and also prevents the energy from re-entering the system due to the periodic boundary conditions. A constant temperature boundary condition is effectively imposed, which is representative of a much bigger lattice surrounding the simulation domain and acting as a thermal reservoir. The size of the simulation domain is different for each ion species and energy and is chosen such that size effects are negligible in all directions. A Berendsen thermostat [26] is used for controlling the temperature during the ion impact, annealing, and initial equilibration period.

All the irradiation simulations are performed at room temperature (300 K) and second-order velocity-Verlet scheme is used for time integration. First, the system is equilibrated to this temperature for a time of 20 ps, after which, the first ion is introduced into the system from the top boundary according to the angle of incidence and the location of impact. The location of the impact is randomly selected according to the type of simulation. These details are described alongside the irradiation results in Sec. V. The polar incidence angle was chosen to be 7.5° in order to avoid channeling effects. The ion impact is considered complete once the temperature of the system has equilibrated to 300 K after the initial spike. The simulation is continued for an additional 1 ps to ensure that any defect configurations have reached an energy minimum, and any material sputtered out-of-plane has time to leave the system.

Ion-irradiation simulations are characterized by widely varying energies and velocities. During the initial phase of the irradiation, extremely high velocities are encountered, leading to the requirement of a very small time step size in order to adequately resolve all the collision dynamics. Once the energy of the ion has been dissipated, the maximum velocities in the system fall by orders of magnitude. Using a single time step size for the entire simulation would lead to unnecessary computational expense. Thus an adaptive time-stepping scheme was implemented based on the recommendation of Nordlund [21], where the new time step size is chosen according to

$$\Delta t_{\text{new}} = \min\left(\frac{k_1}{v_{\max}}, \frac{k_2}{(Fv)_{\max}}, 1.2\Delta t_{\text{old}}, \Delta t_{\text{threshold}}\right). \quad (10)$$

The time step size is chosen based on the maximum velocity and the product of the force F and velocity v. The quantities k_1 and k_2 are constants, whose values were taken from Ref. [21]. In addition, the time step was not allowed to vary more than 20% of the previous value so as to avoid sudden large variations in Δt. Finally, the time step size was never allowed to increase beyond a threshold value, which was specified as 0.1 fs for all the simulations.

In typical ion-irradiation experiments, the time between two ion impacts at nearby locations is on the order of microseconds. At the current temperature, annealing of the formed defects may occur over time spans that are too long to be explicitly represented in MD simulations. In addition, diffusion of defects (both interstitials and vacancies) is also possible. However, both of these effects are expected to be most prominent in the first few picoseconds after the impact during the thermal spike generated from the energy of ion impact. Thus after the ion impact, the system is annealed at the specified temperature using a time step size of 1 fs for a total of 70 ps, before the next ion impact. Annealing and diffusion effects occurring over longer time scales are not captured.

This study examines the defect formation and characteristics resulting from irradiation with four different ions, namely Ne(10), Ga(31), Xe(54), and Pt(78). Three separate energies were considered for each ion species as shown in Table II. The energies for different species were chosen in order to obtain a similar penetration range. First, single ion impact events were performed for all twelve cases (four ions species and three energies for each) in order to establish the characteristics of single impact defects. Next, the behavior of the target system under a more realistic case of continuous bombardment by

TABLE II. Range of energies investigated for each ion species.

Ion species	Z	Energies (keV)		
Neon (Ne)	10	0.75	1	1.5
Gallium (Ga)	31	3	4	5
Xenon (Xe)	54	4	5	6
Platinum (Pt)	78	5	7.5	10

multiple ions is investigated and the results are compared with the single impact simulations. The effect of fluence is then investigated for the continuous irradiation case using a fixed beam diameter of 5 nm. Finally, the effect of varying the beam diameter for a fixed fluence is examined for a single case of Xe ion at an energy of 5 keV.

III. CHARACTERIZATION OF DEFECTS AND STRUCTURAL PROPERTIES

Modification of the material properties may be connected to a number of defect configuration characteristics, including defect density, diameter of the defective region, defect distribution function, etc. Hence a wide range of defect characteristics are presented here, in order to facilitate the calculation of a spectrum of material properties and also establish a connection between defect characteristics and experimental design parameters using this irradiated material information. A brief description of the different defect characteristics employed in this study is presented below.

A. Quantification of the defects

The defective region produced in the lattice during the collision cascade of an energetic ion bombardment is complex, thus its characterization is not a straightforward task. A commonly used method is to characterize the atoms as clusters of vacancies and interstitials, and obtain quantitative information regarding the total number of defective atoms in the system. Such a method is adopted in this study, where the defects are identified using the nearest-neighbor distance spheres. A lattice position is characterized as a vacancy if no atom is present within a sphere of radius equal to half the nearest-neighbor distance, and an atom is considered interstitial if it is not present within half the nearest-neighbor distance of a lattice site. The total number of defects (N_{defects}) is the sum of the vacancies (N_{vac}) and the interstitials (N_{inter}). Although this characterization is not physically appropriate in highly disordered regions, it nevertheless provides a quantitative means of comparing the damage produced by varying the processing parameters. Other criteria have been employed in the literature to define the cutoff for identifying the vacancies and interstitials, such as the Lindemann radius or Wigner-Seitz-cell-Voronoi polyhedron, or using a potential energy threshold. It has been shown, however, that although the number of defects obtained with the different criteria can vary widely, the ratio of the defects predicted by each criteria are approximately the same [11]. Hence the trends observed in the values are expected to be consistent regardless of the specific criteria employed.

B. Characterization of the defective region

In order to define the extent of the defective region, it is cast as a cylindrical region with a diameter D describing the radial extent and height H describing the depth of damage. The diameter is calculated based on the radial distance of the farthest defect from the point of impact. The height is determined by the distance of the defects from the top surface. By these definitions, the cylindrical domain completely envelopes the damaged region, and the rest of the target is pristine. However, not all regions inside the cylinder are damaged and as a result, this cylinder contains a significant portion of pristine material. Area (ρ_{area}) and volumetric (ρ_{vol}) defect densities are also calculated using these quantities based on the following definitions:

$$\rho_{\text{area}} = \frac{N_{\text{defects}}}{\frac{\pi}{4}D^2}, \tag{11}$$

$$\rho_{\text{vol}} = \frac{N_{\text{defects}}}{\frac{\pi}{4}D^2 H}. \tag{12}$$

C. Defect distributions

All of the defect region properties defined above are effective quantities. In order to understand the distribution of the defects inside the damaged region, the defect radial distribution function (DRDF) and the defect depth distribution function (DDDF) are also computed. Both these quantities are calculated in MD using the histogram or binning method [27]. The DDDF is calculated by counting the number of defects present within the volume $A\Delta z$ using linear bins along the height (or depth), where A is the area along the x–y direction and Δz is the bin size. The DDDF is normalized by the total number of atoms present within this volume in a pristine lattice.

For computing the DRDF, a planar radial bin is required, and the number of defects present within the annular region of volume $2\pi H r \Delta r$ is calculated. Δr is the size of the radial bin and H is the height of the system. However, due to the crystalline nature of the silicon lattice, the number of atoms present within a radial bin are characterized by sharp peaks and valleys. This causes the number of defects within the bins to vary widely, thus leading to large fluctuations in the DRDF. Hence the DRDF is normalized using the total number of atoms present inside the particular bin in a pristine lattice:

$$\text{DRDF}(r) = \frac{n_{\text{defect}}(r : \Delta r)}{n_{\text{pristine}}(r : \Delta r)}. \tag{13}$$

Here, $n_{\text{defect}}(r : \Delta r)$ represents the number of defects inside a particular bin within the region $r - \Delta r/2$ and $r + \Delta r/2$. $n_{\text{pristine}}(r : \Delta r)$ is the total number of atoms present within the same bin in a pristine lattice.

D. Amorphous pockets

The primary defect formation mechanism during energetic ion irradiation occurs through local melting of the cascade region resulting from a thermal spike and subsequent re-solidification into amorphous pockets [9,28,29]. These amorphous pockets are categorized as defect clusters. Clusters are identified starting with a single defect, and all defects present within one bond distance of the first defect is included in the

cluster. This process is carried out until all defects present within the specified distance of any defect in the cluster are found. The distribution of defects among the cluster sizes, and other properties such as the total number, average size are computed. In addition, the excess or deficit of atoms within each cluster is also calculated. These properties are used to provide insight into the process of defect formation and cascade dynamics.

IV. CALCULATION OF THERMAL CONDUCTIVITY

The lattice thermal conductivity of the damaged Silicon system is calculated with classical equilibrium molecular dynamics using the Green-Kubo method [30,31]. The Green-Kubo formulation uses the fluctuations in the heat current for computing the thermal conductivity via the fluctuation-dissipation theorem:

$$\kappa(\tau_m) = \frac{1}{k_b V T^2} \int_0^{\tau_m} \langle \boldsymbol{J}(\tau)\boldsymbol{J}(0)\rangle d\tau. \tag{14}$$

Here, k_b is the Boltzmann's constant, V is the volume, and τ is the time. $\boldsymbol{J}$ is the heat current and its fluctuation is expressed by the heat current autocorrelation function $\langle \boldsymbol{J}(\tau)\boldsymbol{J}(0)\rangle$. The heat current $\boldsymbol{J}$ for the three-body Tersoff potential is expressed as [32]

$$\boldsymbol{J} = \sum_i \left[\boldsymbol{v}_i \varepsilon_i + \sum_{j\neq i} \left(\frac{1}{2} \boldsymbol{r}_{ij}.(\boldsymbol{F}_{ij}.\boldsymbol{v}_i) + \frac{1}{6} \sum_{k\neq i,j} (\boldsymbol{r}_{ij} + \boldsymbol{r}_{ik}).(\boldsymbol{F}_{ijk}.\boldsymbol{v}_i) \right) \right], \tag{15}$$

where $\boldsymbol{v}_i$ is the velocity of the particle i and ε_i is the total energy of the particle, which is defined as the sum of the kinetic and potential energy. The distance between the particles is $\boldsymbol{r}$, and $\boldsymbol{F}_{ij}$ and $\boldsymbol{F}_{ijk}$ are the two- and three-body force terms, respectively.

All the thermal conductivity calculations were performed at 300 K with a time step of 0.05 fs. Further reduction in the time step did not yield any change in the thermal conductivity values during the preliminary studies. First, the system is equilibrated at the specified temperature for 20 ps using the Berendsen thermostat [26]. The system is then allowed to evolve in the microcanonical ensemble (NVE) for an additional 20 ps, before recording the heat current information for a simulation time of 6 ns. Higher total running times did not alter the thermal conductivity values. An additional convergence study for the size effect of the thermal conductivity calculations showed that the 8×8×8 domain cell was sufficient to get converged values for thermal conductivity of silicon, consistent with the literature [32–34]. Hence, for all the cases, a domain size of at least eight unit cells were used along each of the directions. For each case, ten independent simulations with different initial velocity configurations were performed and the final averaged thermal conductivity values are reported. The thermal conductivity in this study is obtained from direct numerical integration of the heat current auto-correlation function over the specified correlation time. The thermal conductivity as a function of the correlation time for pristine silicon is shown in Fig. 2. The flattening of the curve essentially implies that the auto-correlation has decayed to zero. The error bars indicate the standard deviation in the thermal conductivity values computed from the ten independent simulations. The calculated thermal conductivity of Silicon at room temperature is around 273 $\mathrm{W\,mK^{-1}}$, which is almost twice that of the experimentally observed value of around 150 $\mathrm{W\,mK^{-1}}$ [35]. This difference is attributed to the overly stiff description of the Silicon bonds by the Tersoff potential [36,37].

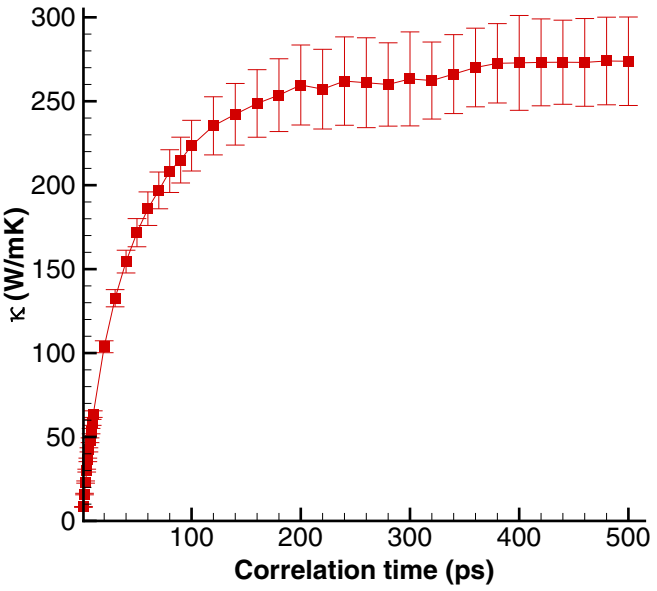

FIG. 2. Calculated thermal conductivity for pristine silicon system at 300 K.

In order to calculate the thermal conductivity of the defective system, the complete defective region is placed within a pristine lattice and periodic boundary conditions are employed. This is representative of a lattice that has been irradiated with ions periodically in the x and y direction. Such a method effectively provides a way of qualitatively comparing the effect of the different processing parameters on the thermal conductivity. Due to the high anisotropy in the distribution of the defects in the x/y and z directions, the thermal conductivity values reported are only along the x and y directions: $\kappa_{\mathrm{avg}} = (\kappa_x + \kappa_y)/2$.

V. RESULTS

A. Comparison of single and multi-ion impacts: effect of energy and ion atomic number

In this section, the effect of ion atomic number and energy on the properties of the defective region is investigated for the case of single and multi-ion bombardment of the lattice. Simulations were first performed for a single ion impacting the 3D silicon lattice in order to understand the basic defect formation characteristics of each of the ions. The location of the ion impact was randomly selected within the minimum irreducible area of the lattice near the center of the system as shown in Fig. 3(a). A total of 250 simulations were performed for each ion and energy in order to obtain sufficient statistics.

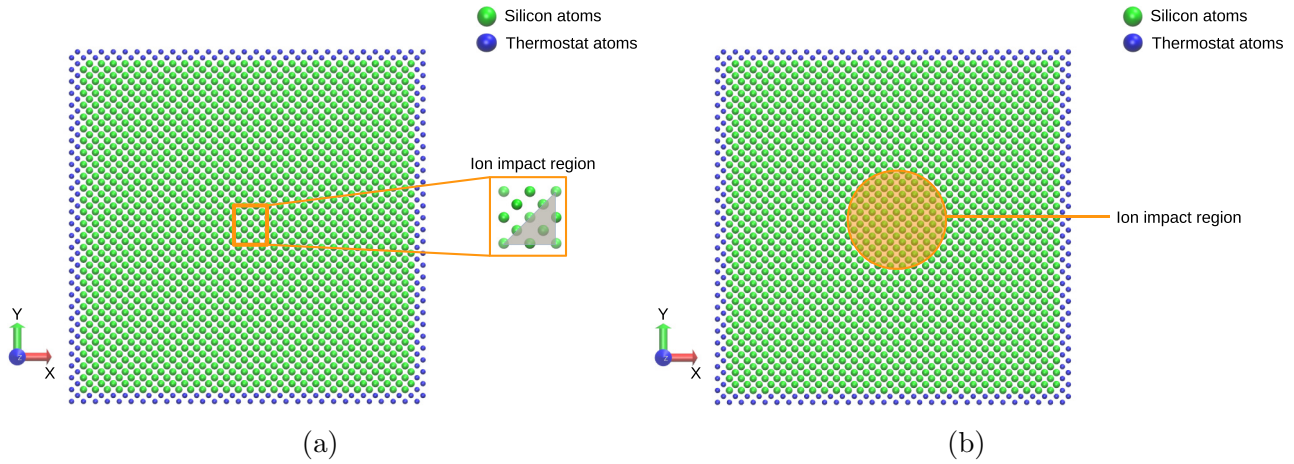

FIG. 3. Schematic illustration of the top view of the 3D simulation setup for (a) single-ion impact and (b) multi-ion impact events. Thermostat atoms are present on the four sides. The ions impact the center of the lattice within the minimum irreducible area as shown in the case of single-ion impacts. During continuous bombardment, successive ions impact the center of the lattice within the given circular area based on a Gaussian-distributed ion beam.

The statistical quantities of interest were found to be insensitive to additional simulations.

For simulations of multi-ion bombardment of the 3D lattice, the location of the successive ion impacts was chosen randomly based on a two-dimensional Gaussian distribution within a specified beam diameter [Fig. 3(b)] similar to that of a FIB apparatus. For the study in this section, all the multi-ion impact simulations were carried out for a fixed beam diameter of 5 nm and a fluence of 2.54×10^{13} ions cm^{-2} corresponding to a total of five ions striking the lattice. A total of 50 independent cases of the complete irradiation process with multiple ions striking the system is performed to obtain converged statistics for all the fluences presented here. Again the statistics were found to be insensitive to an increase in the number of simulations.

Figures 4–6 show the perspective view of representative defective regions produced through ion bombardment in Silicon lattice. Figure 4 presents the defective lattice obtained from irradiation of Pt 10 keV single-ion impact and multi-ion (five ions) impact events. Figure 5 showcases the effect of ion atomic number on the defective regions produced by 5-keV energy ions of Ga(31) and Pt(78). Finally, the effect of ion energy is shown in Fig. 6 for single ion impact events of Xe 4 keV and 6 keV ions.

Results from the analysis of single and multi-ion impact studies are presented in Fig. 7. As expected, we observe a monotonic increase in the number of defects with both the ion energy and atomic number, consistent with the literature [9,38]. The ratio of the number of defects between the multiple and single ion case remains almost constant at 5 for all the ions and energies (for the ranges considered here). The energy of the ion is absorbed into the lattice leading to the collision cascade which reconfigures the system and eventually leads to

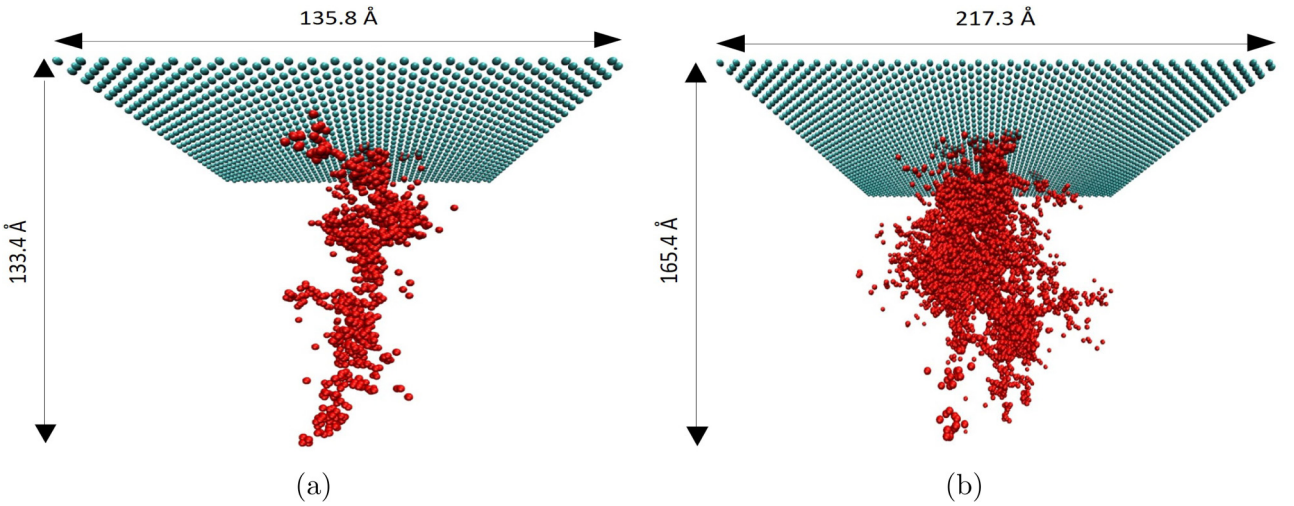

FIG. 4. Perspective view of a representative defective silicon lattice produced by irradiation of (a) Pt(78) 10-keV single-ion and (b) Pt(78) 10-keV multi-ion (five ions) impact events. The pristine regions are transparent, while the defective and surface atoms are indicated by red and cyan, respectively.

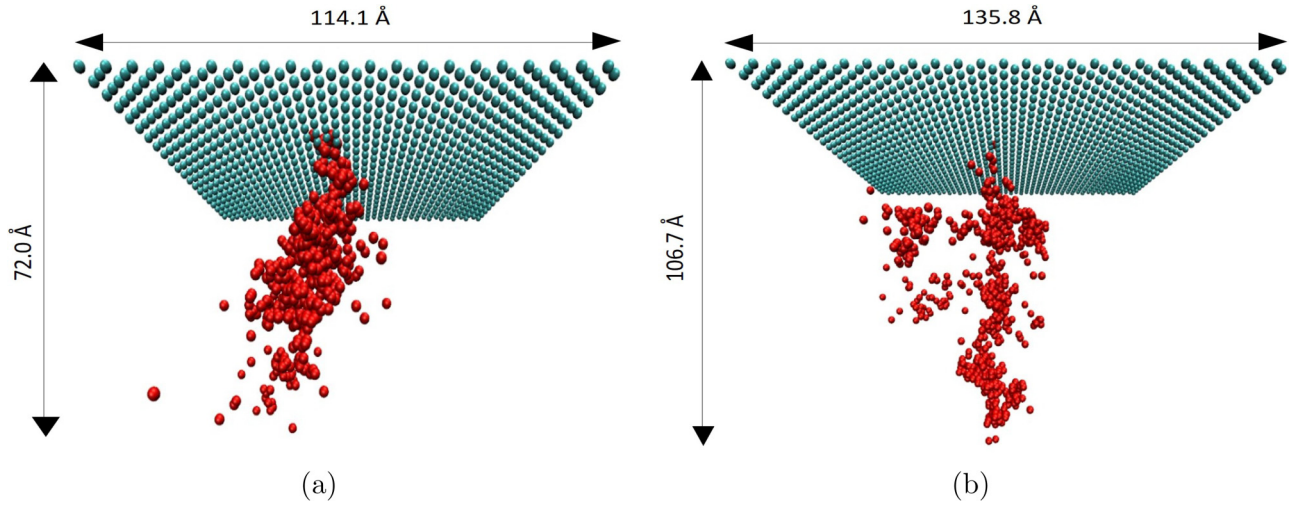

FIG. 5. Perspective view of a representative defective silicon lattice produced by irradiation of (a) Ga(31) 5-keV single-ion and (b) Pt(78) 5-keV single-ion impact events. The pristine regions are transparent, while the defective and surface atoms are indicated by red and cyan, respectively.

heat dissipation through the creation of lattice phonons. Each successive ion impact on the lattice dissipates the energy in a similar manner resulting in a (nearly) linear increase in the defects with the number of ions.

Although the diameter of the defective region increases with energy for all the cases examined, the ratio of the defect diameters generated by single and multi-impact events decreases with both ion atomic number and energy. During multiple ion impacts, there is significant overlap of the defective regions generated by the ions. This is clearly seen from Fig. 4(b) (multi-ion), where there are no distinct defective regions from the five different ion impacts due to the complete overlap. Overlapping of the defective regions become more pronounced for the cases with larger defective regions in the single impact studies (higher ion atomic numbers and energies). Hence a disproportionate scaling of the defect diameters compared to the number of defects is observed with increasing fluence for different ion atomic numbers and energies.

In the case of single impacts of Ne and Xe ions, the diameter of the defective region varies with energy in such a way that the area density ρ_{area} reaches a maximum and then decreases. In the case of Ga and Pt ions, this is not observed and the area denisty monotonically decreases. However, with increasing ion atomic number, ρ_{area} is found to continually increase. This is shown in Fig. 5 and can also be seen by comparing 5-keV case of Ga, Xe, and Pt. Owing to the disproportionate scaling of the diameter of defective region in comparison with the number of defects, a monotonically increasing trend is observed in the area density of defects ρ_{area} with energy for all the ions in the multi-impact case. The effect of ion atomic number on ρ_{area} remains consistent (monotonically increasing) with the single impact study.

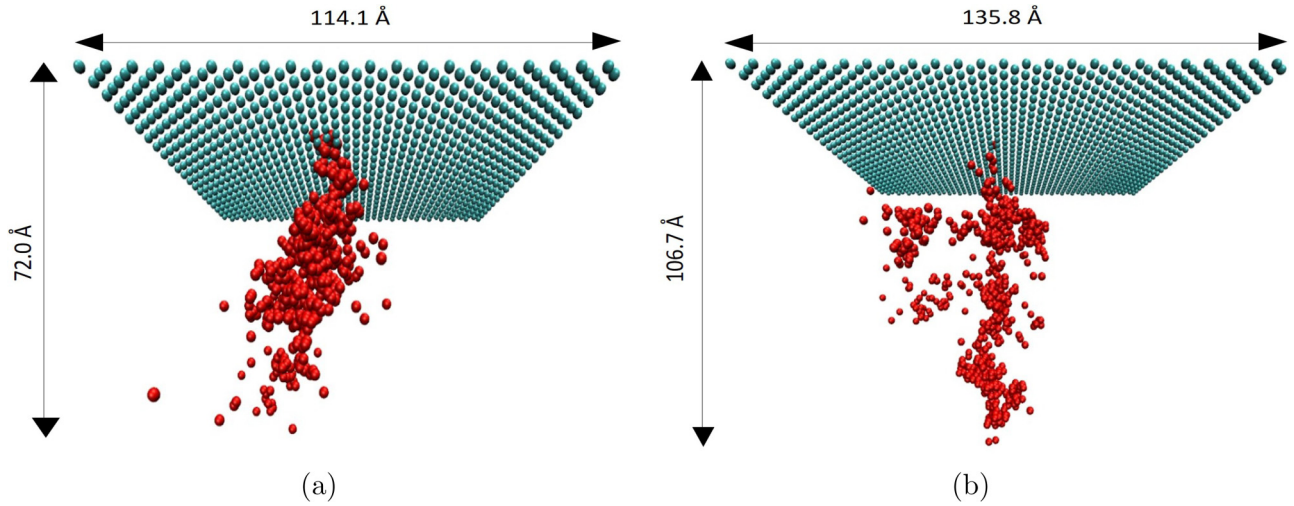

FIG. 6. Perspective view of a representative defective silicon lattice produced by irradiation of (a) Xe(54) 4 keV single-ion and (b) Xe(54) 6 keV single-ion impact events. The pristine regions are transparent, while the defective and surface atoms are indicated by red and cyan respectively.

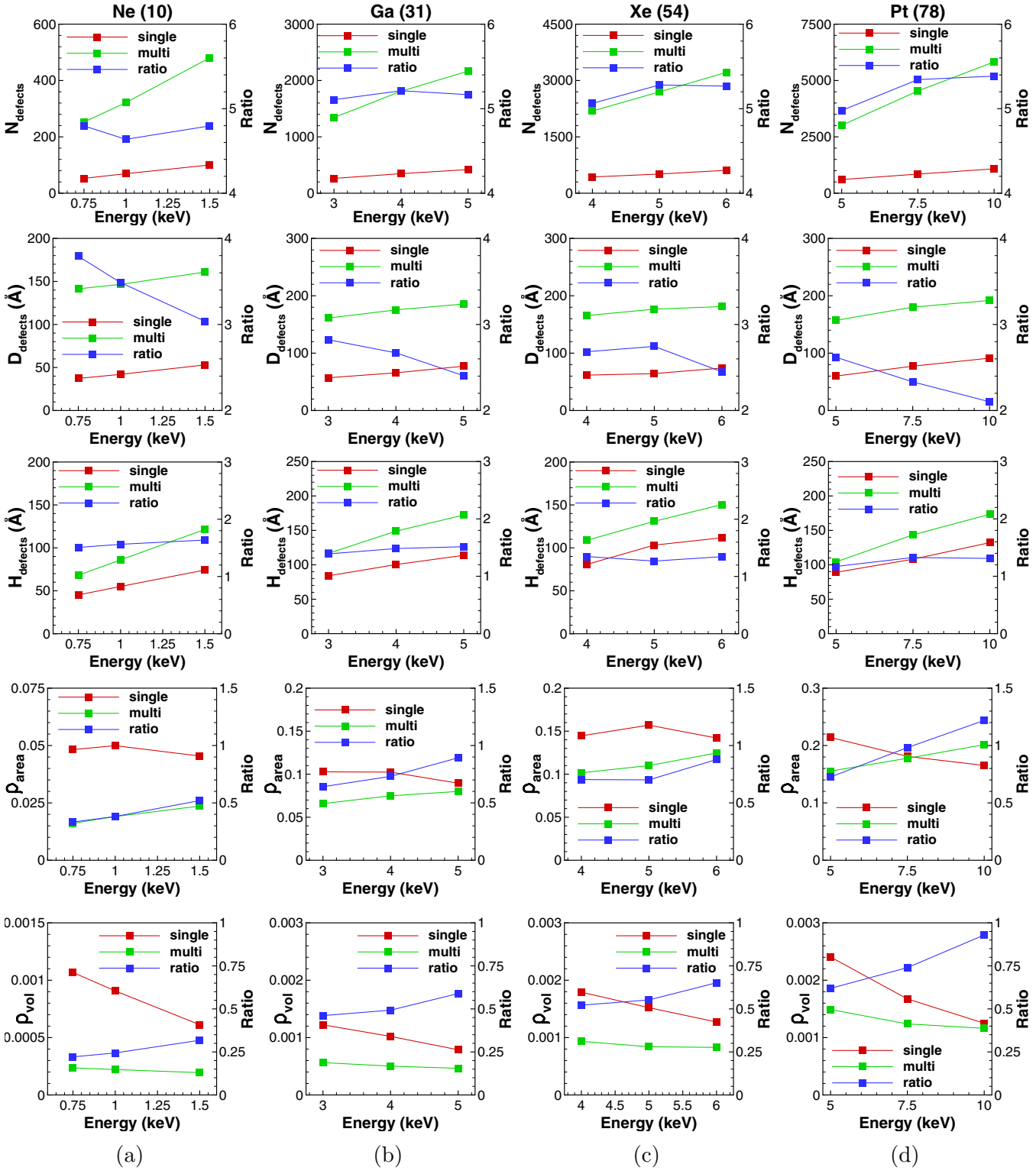

FIG. 7. Average values for number of defects (row 1), diameter (row 2), height (row 3), area density (row 4), and volumetric density (row 5) of the defective region for single-ion impact (red) and multi-ion impacts (green) irradiation of silicon with (a) Ne(10), (b) Ga(31), (c) Xe(54), and (d) Pt(78) ions of different energies. The multi-ion impact case corresponds to a fluence of 2.54×10^{13} ions cm^{-2} and a beam diameter of 5 nm. The ratio of each of the properties (blue) are also plotted on the secondary axis on the right for comparison.

For both the single and multi-impact cases, the height of the defective region is found to increase with the energy for all ions studied (Fig. 7, row 3). This can be attributed to the greater penetration depth of the ions with larger energies [9,28]. Also the depth (height) decreases with increasing ion atomic number owing to the stronger interaction potential (discussed below).

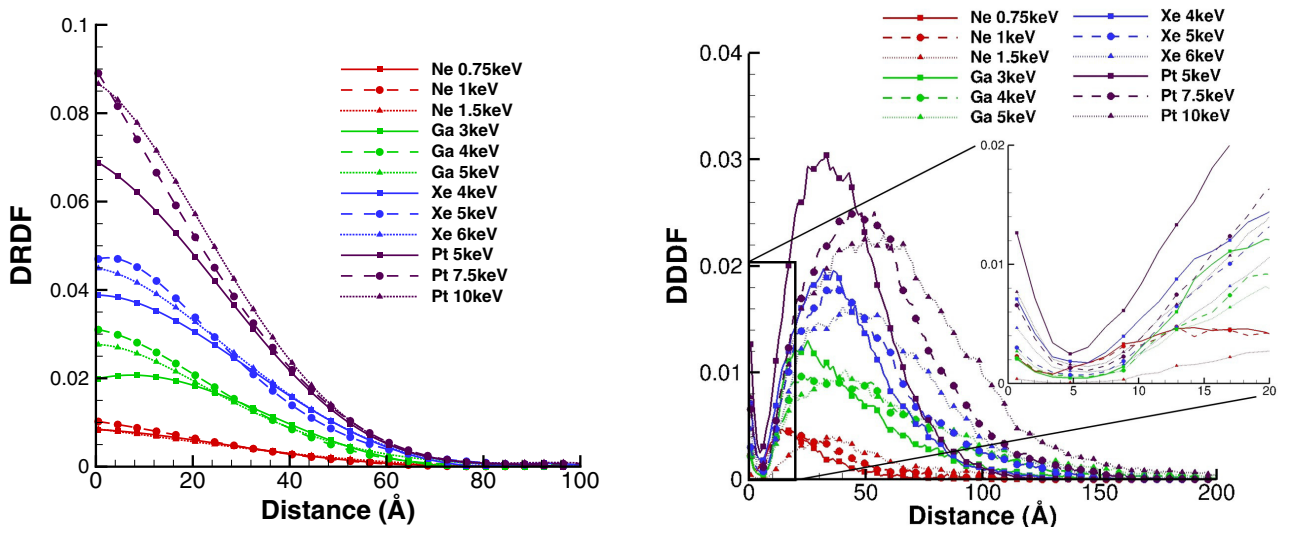

FIG. 8. (a) Defect radial distribution function (DRDF) and (b) Defect depth distribution function (DDDF) for irradiation of Silicon with Ne(10), Ga(31), Xe(54), and Pt(78) ions of multiple energies at a fluence of 2.54×10^{13} ions cm^{-2} and a beam diameter of 5 nm.

The ratio of the heights between single and multi-impact cases is approximately constant with energy for each ion and appears to marginally decrease with ion atomic number.

The volumetric density ρ_{vol} decreases with energy for all the cases examined. This behavior is explained by the much larger defective regions obtained in the case of higher energy impacts, which consequently leads to sparsely populated defective region, and lower volumetric defect densities (Fig. 6). Thus a more compact defective region with a small volume and high defect density can be produced by using ions of lower energies and large atomic numbers.

The atomic number of the ions is identified to be the most important parameter for controlling the density of defects within a given region. Lower atomic number ions should be utilized when a long, but sparse defective region is desired, while ions with higher atomic numbers should be chosen for creating a concentrated region of defects. The role of energy as a tunable parameter is to increase the area density, while decreasing the volumetric density. Varying the ion energy thus allows for the tailoring of physical properties dependent on area density [39–41] (e.g., directional conductivity, resistivity, etc.) or properties dependent on volumetric density [4,42,43] (e.g., hardness, crystallinity, etc.).

The increased penetration of the higher energy ions is responsible for opposite trends observed for the area and volumetric densities. Although volumetric density decreases with energy for both the single-ion and multi-ion impact cases, the rate of decrease is however, not similar. This is evident from the plot of the ratio of volumetric defect densities, which continually increases with both energy and ion atomic number. This is mainly due to the disproportionate scaling of the defect diameters resulting from the overlap of the defective regions.

From this analysis, we can conclude that the results from single ion impacts cannot be directly extrapolated to predict the behavior of the lattice under continuous bombardment of multiple ions. For the range of conditions examined, the total number of defects scales linearly with the number of impacts. Characteristics of the defective regions including diameter, height and density exhibit a more complex behavior depending on whether single or multi-ion impacts are considered. Hence, for analyzing damage due to irradiation and comparison with experiments, multi-ion impact simulations are necessary.

Figure 8(a) presents the defect radial distribution function (DRDF) for the multi-ion impact case for all the different ions and energies considered. The DRDF is observed to uniformly decrease with the radial distance for all the ions and energies. Similar to the defect densities, the effect of ion atomic number is much more prominent than the effect of energy on the DRDF. In addition, both the vacancies and interstitial distributions were found to be very similar and follow closely the defect distribution. The defect depth distribution function (DDDF) is plotted in Fig. 8(b). A self similar profile is observed for all the ions and energies. The distributions of vacancies and interstitials are also very similar and closely resemble the DDDF, except near the surface where more vacancies are present. Within the lattice, a singly peaked distribution of the defects is found close to ion penetration depth consistent with the Bragg peak distribution [22]. When the ions enter the lattice at high speeds, the energy interaction/exchange with the target nuclei are lower owing to the reduction in the nuclear scattering cross sections with increasing kinetic energy. A significant portion of the energy loss at higher speeds are due to collisions with electrons (electronic stopping). As the ions decelerate, the interactions with the target nuclei increase leading to lattice defects and thus the peak in the DDDF is observed close to the penetration depth of the ions. Both the ion atomic number and energy influence the magnitude and position of the peak. Higher energies tend to shift this peak further into the lattice, while larger ions at the same energies have peaks closer to the surface. This is because of the greater interaction potential of the larger ions [9], resultant of the form of the

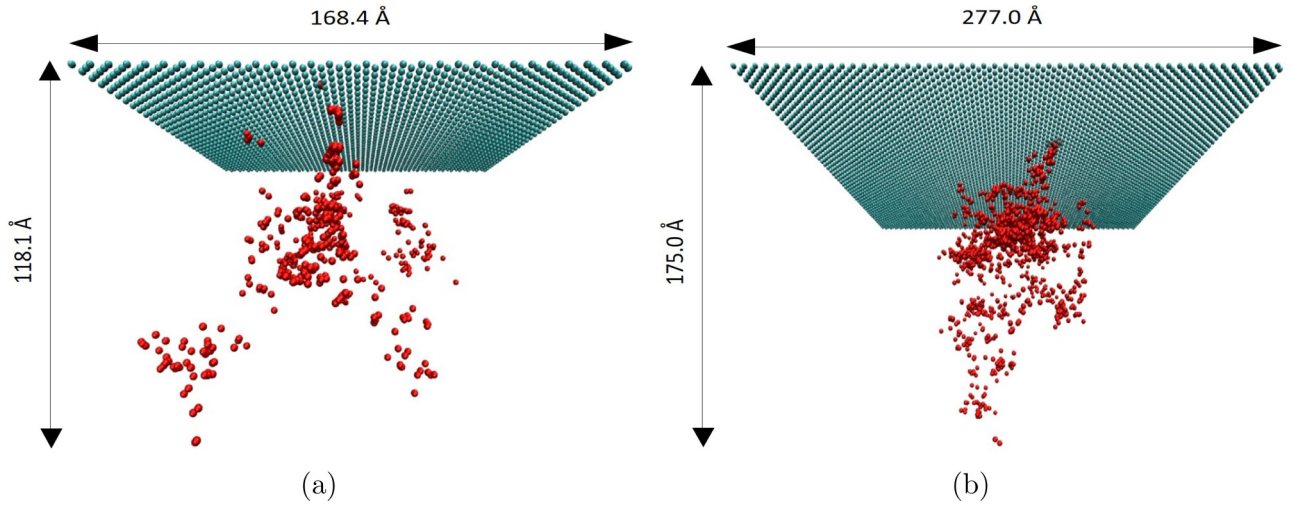

FIG. 9. Perspective view of a representative defective silicon lattice produced by irradiation of Ne(10) 1.5-keV ions at a fluence of (a) 2.54×10^{13} and (b) 7.64×10^{13} ions cm^{-2}. The pristine regions are transparent, while the defective and surface atoms are indicated by red and cyan, respectively.

ZBL potential [Eq. (1)]. The magnitude of the peak increases with the ion atomic number and reduces with the energy [9,38] consistent with the variation of the volumetric defect density. An additional small peak in the distributions is observed near the surface owing to the sputtering effects and also due to the lower energies required for defect formation near the surface. This peak is found to decrease in magnitude with increasing energy of the ions. Again, the reduced interaction time of the ion with the surface atoms resulting from the higher velocities is responsible for this decrease in magnitude.

These detailed DRDF and DDDF distributions provide the necessary information to characterize physically representative defective regions for subsequent irradiated material analysis. Such information can then be directly employed within theoretical and computational calculations to investigate the effect of the damaged regions on physical (structural, electronic, thermal, magnetic, etc.) properties of the system [44–49].

B. Effect of fluence

In this section, the effect of fluence on the characteristics of the defective region is studied for all the twelve cases considered above (four ions at three energies each). A total of 15 ions were used to impact the lattice, and this complete irradiation process was independently carried out 50 times to gather adequate statistics. The characteristics of the defective region is plotted in Fig. 10 after the impact of 5, 10, and 15 ions corresponding to a fluence of 2.54, 5.09 and 7.64×10^{13} ions cm^{-2}, respectively. Figure 9 shows defective regions of the silicon lattice produced by the bombardment of the same ion (Ne 1.5 keV) at different fleunces. Figure 9(a) corresponds to a fluence of 2.54×10^{13} ions cm^{-2} and Fig. 9(b) is at a fleunce of 7.64×10^{13} ions cm^{-2}.

1. Formation of amorphous pockets

In order to gain further insight to the process of defect formation and cascade dynamics, the properties of the defect clusters are analyzed. First, the effective excess of atoms within each cluster was found to be close to zero for all cases with the maximum value not exceeding 10. This indicates that the vacancies and interstitials are uniformly distributed within the clusters and are not grouped together. Table III presents the average cluster size and the fraction of defects present in clusters of size greater than 10. The average fraction of isolated single and Frenkel pair defects for all the cases considered is shown in Table IV. Note that the term Frenkel pair is used here to refer to interstitials and vacancies that are within one bond distance. This can be thought of clusters of size two without any excess or deficit of atoms. We notice that only a small percentage of the defects are isolated, most of the defects are present in clusters. This is consistent with the short replacement collision sequences(RCS) reported for semiconductors [50,51]. Further the fraction of isolated single defects is consistently greater (almost twice) than the Frenkel defects. Thus, although the RCS is small in silicon compared to metals, it is long enough to displace the atoms from their original location by a distance greater than one bond distance.

As the ion atomic number increases, the average cluster size becomes greater. This is because the lower mass ions tend to penetrate further into the lattice, leaving behind a wake of isolated and small cluster defects. Interestingly, the cluster size does not seem to depend on the energy of the ion. This suggests that the nature of the collision sequence and the defect formation and the behavior of cascades is not influenced by the energy of the ion (for the ranges presented here). With increasing fluence, the cluster size rises and the number of isolated defects falls. This could be an effect of two factors. Firstly, there is greater overlap of cascade of multiple ions, thus leading to more clusters and smaller number of isolated defects. Secondly, the defective regions that are created are less stable than pristine regions and therefore are more susceptible to further damage as more ions strike the lattice, giving rise to more defects in clusters.

TABLE III. Average cluster size and fraction of defects within clusters larger than 10 in silicon for the range of ion energies, atomic number, and fluence.

		Average cluster size Fluence ($\times 10^{13}$ cm^{-2})			Fraction of defects in clusters larger than 10 (%) Fluence ($\times 10^{13}$ cm^{-2})		
Ion	Energy (keV)	2.54	5.09	7.64	2.54	5.09	7.64
	0.75	4.4	4.7	5.1	54.0	55.4	59.6
Ne	1.0	4.6	4.9	5.3	55.6	58.3	61.5
	1.5	4.6	4.6	5.3	54.6	55.7	61.7
	3.0	9.4	11.7	15.1	79.6	83.3	86.9
Ga	4.0	9.3	11.9	14.1	79.2	83.9	85.9
	5.0	9.2	11.6	14.2	78.6	83.2	85.8
	4.0	16.7	24.3	28.4	88.8	91.8	93.1
Xe	5.0	16.4	23.0	27.2	88.3	91.5	92.8
	6.0	15.8	22.5	25.5	87.5	91.3	92.2
	5.0	24.6	33.8	42.0	92.2	94.1	95.2
Pt	7.5	24.1	30.6	35.7	91.9	93.5	94.3
	10.0	22.3	29.1	36.1	91.0	93.2	94.4

2. *Effective properties of the defective regions*

As evident from Fig. 10, the number of defects, diameter and height of the defective region show a monotonic increase with energy for all the ions at all fluences. The number of defects shows a (nearly) linear increase with the fluence. This is consistent with the reasoning mentioned in the last section that the energy of each successive ion is dissipated into the lattice in a similar manner and resulting in a (roughly) linear increase of defective atoms on average. From the results in current and previous section, reasonable estimation for the number of defects for other ions, (reasonable) energy and fluence ranges can be obtained.

The diameter and height of the defective region also increases monotonically with fluence, but the rate is much less pronounced in comparison with the number of defects. In addition, both the diameter and height also decrease with the ion atomic number for the same energy (by comparing the 5-keV case of Ga, Xe, and Pt). The area density (ρ_{area}) and volume density (ρ_{vol}) show opposite trends with energy for all fluences. The quantity ρ_{area} is found to monotonically increase with energy owing to the much steeper growth in the number of defects in comparison with the diameter. However, the ρ_{vol} is observed to decrease with energy indicating that the combined effect of the rise in diameter and height is greater than the increase in the number of defects. This implies that greater ion energies lead to the production of less sparsely populated defective regions owing to the larger penetration and spread, for the energy ranges explored here.

3. *Defect distributions*

The defect radial distribution function (DRDF) and the defect depth distribution function (DDDF) for the different ions and fluences are plotted in Figs. 11 and 12, respectively. As a general trend, the fluence increases the peak magnitude

TABLE IV. Fraction of isolated single and Frenkel pair defects in silicon for the range of ion energies, atomic number, and fluence.

		Isolated single defects (%) Fluence ($\times 10^{13}$ cm^{-2})			Isolated Frenkel pair defects (%) Fluence ($\times 10^{13}$ cm^{-2})		
Ion	Energy (keV)	2.54	5.09	7.64	2.54	5.09	7.64
	0.75	11.4	10.8	10.0	6.0	5.6	5.2
Ne	1.0	11.3	10.2	9.8	5.3	5.2	4.5
	1.5	11.4	11.6	9.7	5.1	5.5	4.6
	3.0	5.6	4.6	3.6	2.8	1.8	1.4
Ga	4.0	5.6	4.5	3.7	2.5	1.9	1.6
	5.0	5.6	4.6	3.7	2.4	1.9	1.6
	4.0	3.2	2.3	2.0	1.3	1.0	0.8
Xe	5.0	3.3	2.4	2.0	1.5	1.1	0.8
	6.0	3.3	2.5	2.1	1.5	1.1	0.9
	5.0	2.2	1.6	1.3	0.9	0.7	0.6
Pt	7.5	2.2	1.8	1.5	1.0	0.8	0.6
	10.0	2.3	1.9	1.5	1.1	0.9	0.6

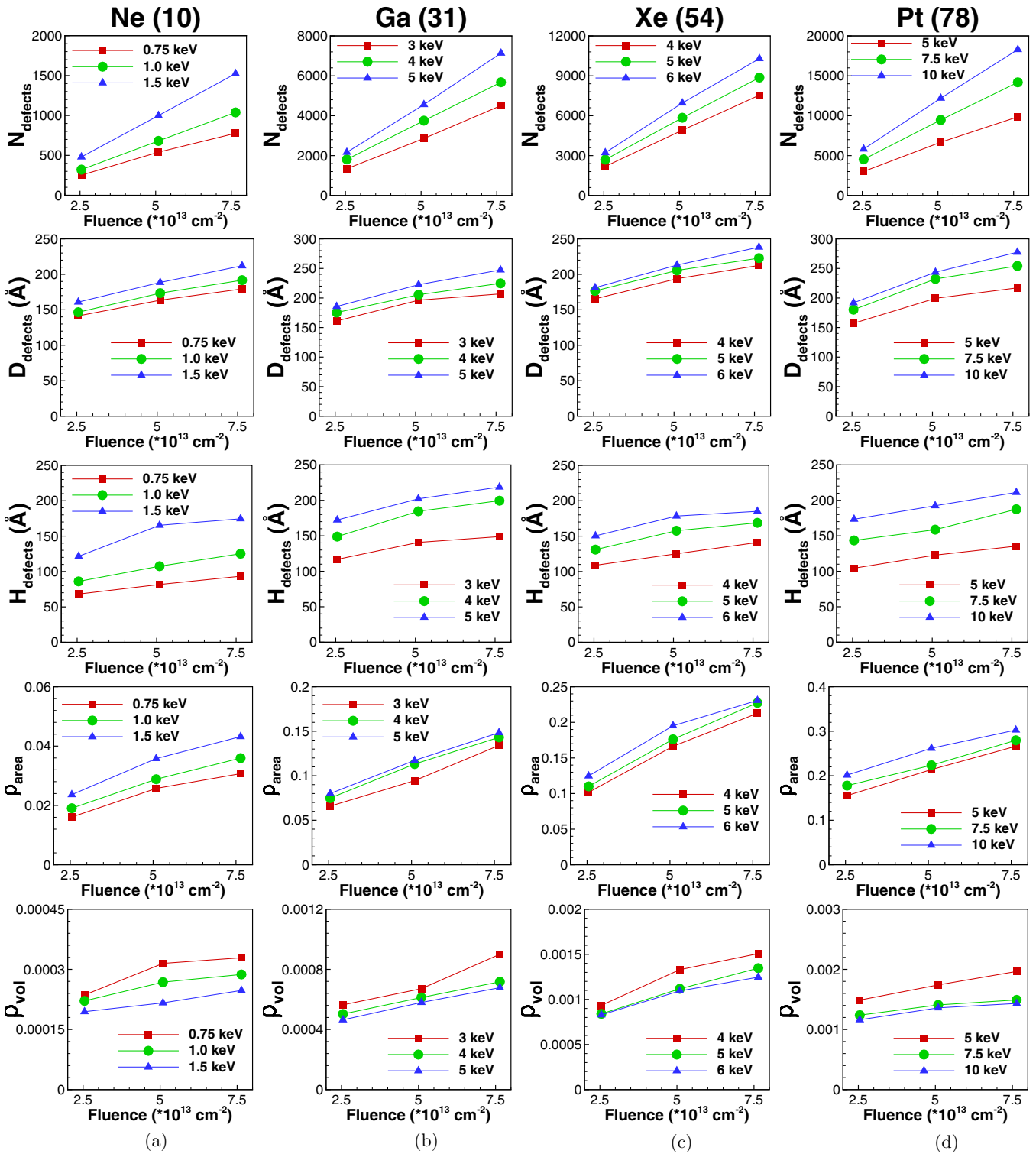

FIG. 10. Average values for: number of defects (row 1), diameter (row 2), height (row 3), area density (row 4), volumetric density (row 5), and thermal conductivity (row 6) of the defective region for continuous irradiation of silicon at multiple fluences with (a) Ne(10), (b) Ga(31), (c) Xe(54), and (d) Pt(78) ions of different energies.

and widens the distribution in the DRDF. For a given fluence, the DRDF of ions with smaller energies have a smaller spread consistent with the trends in the volumetric density. The plots of the DDDF are qualitatively very similar for the different ions. In addition to the ion atomic number (discussed above), the magnitude and position of the peak within the lattice and the spread of the defects along the height is determined by both the energy and the fluence. Higher fluence leads to a wider distribution and gives rise to a larger peak, which is also observed to slightly shift deeper into the lattice. The DDDF of ions with greater energy are characterized by a smaller peak, that occurs at a greater depth and is characterized by a

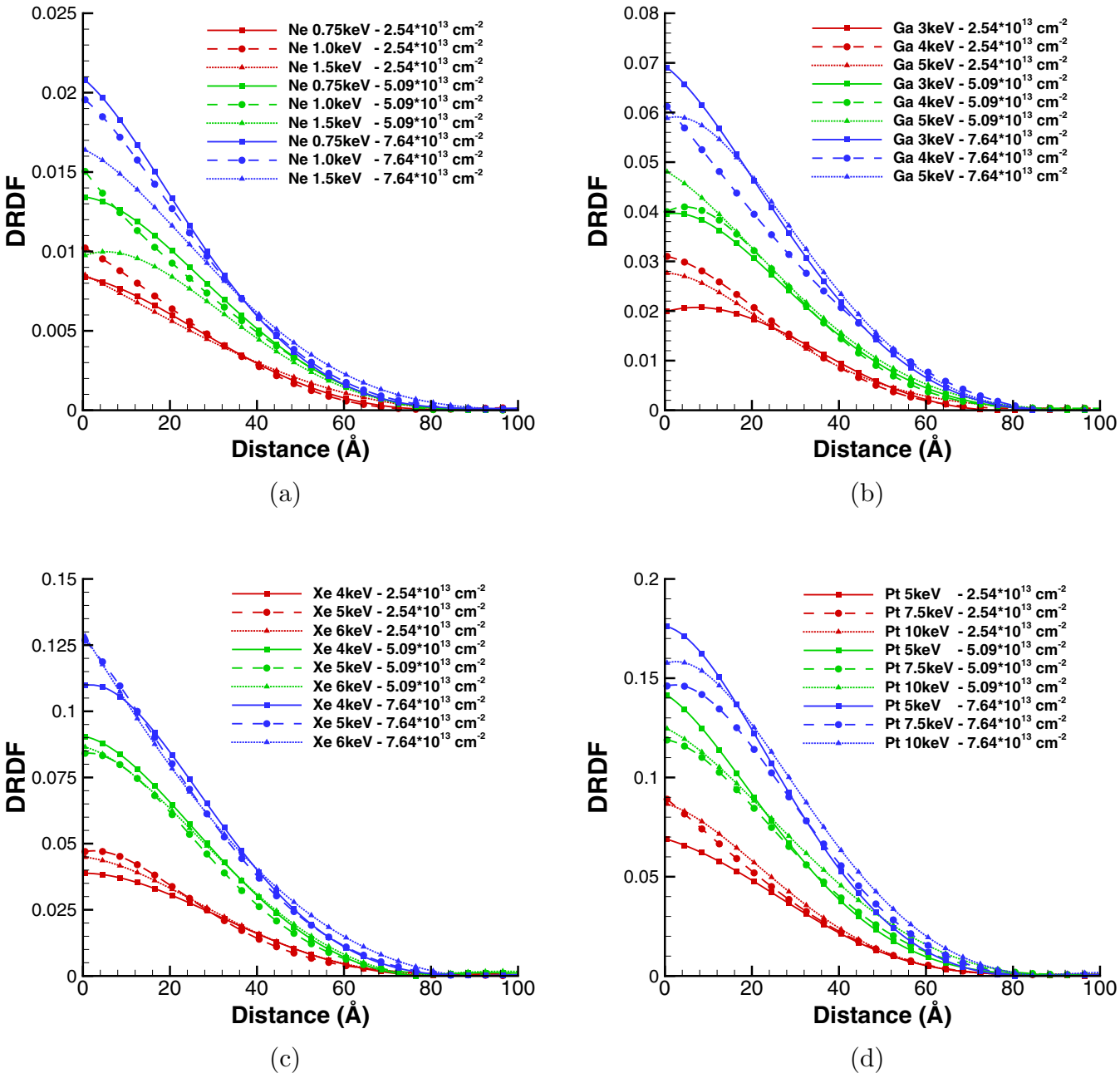

FIG. 11. Defect radial distribution function (DRDF) for irradiation of silicon with (a) Ne(10), (b) Ga(31), (c) Xe(54), and (d) Pt(78) ions of different energies and fluences with a constant beam diameter of 5 nm.

much wider distribution, consistent with the variation in the volumetric defect density.

4. Thermal conductivity

Thermal conductivity is presented next for the multi-ion irradiated material (Fig. 13). For the thermal conductivity calculations, out of the 50 independent runs, the lattice with the defective region most closely resembling the average properties (presented above) is chosen. The complete defective region was placed at the center of pristine lattice of size 400×400 Å^2 for all the cases. The thermal conductivity has negligible variation with the irradiation energy used to create the defects. We note that while higher ion energies produces large defect diameters, resulting in greater phonon scattering; the density of the defects within this region also reduces with increasing energies leading to reduced scattering of phonons. These competing effects result in negligible variation in the thermal conductivity with the energy. The increase in fluence clearly results in a decrease in the thermal conductivity owing to the increase in both the size and density of the defective region.

C. Effect of beam diameter

In all of the simulations in the previous sections, the beam diameter was kept constant at 5 nm (50 Å). The effect of varying the beam diameter on the characteristics of the defective region is examined in this section. Simulations

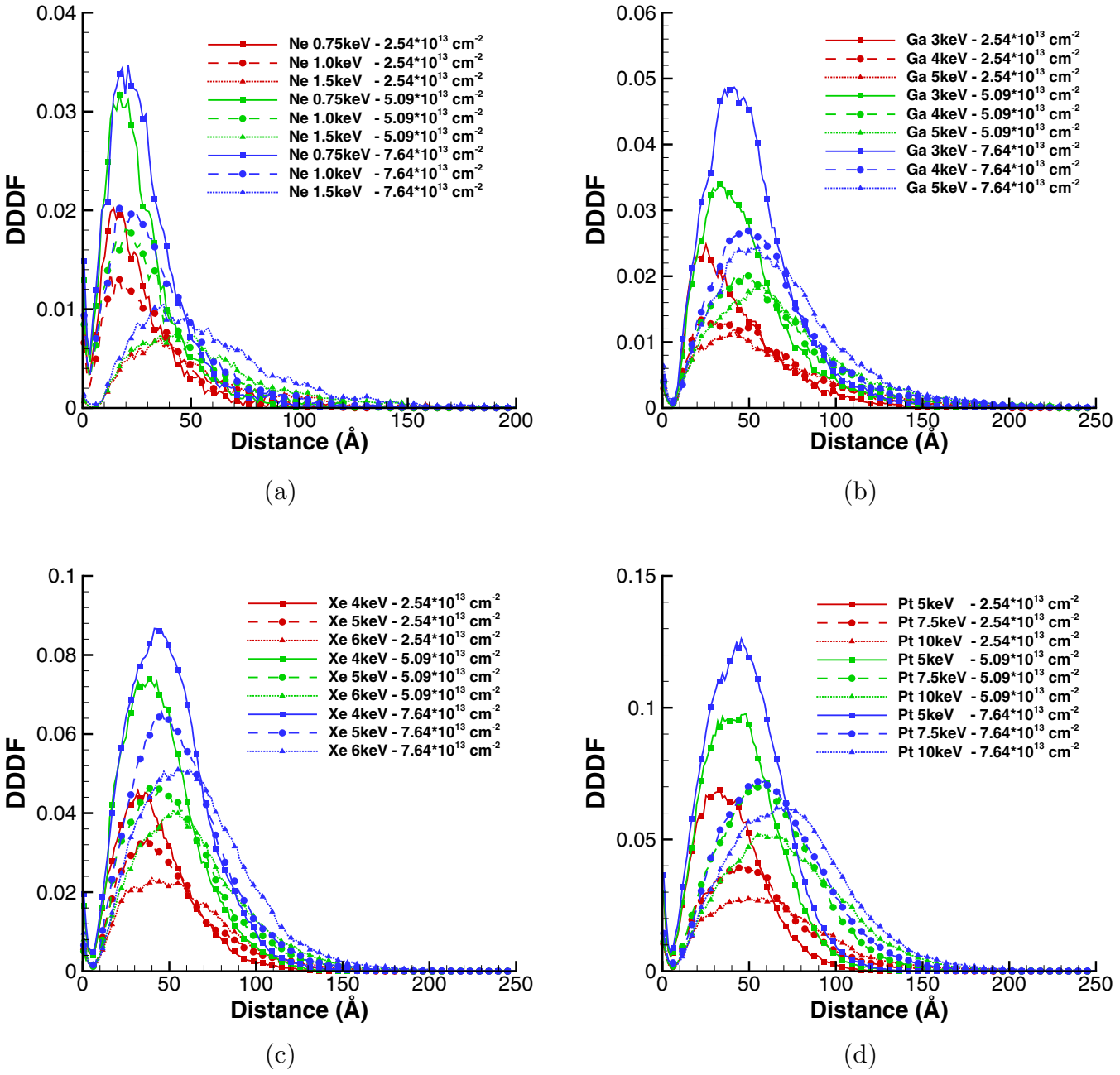

FIG. 12. Defect depth distribution function (DDDF) for irradiation of silicon with (a) Ne(10), (b) Ga(31), (c) Xe(54), and (d) Pt(78) ions of different energies and fluences with a constant beam diameter of 5 nm.

were performed for three different beam diameters of 50, 70, and 100 Å, while maintaining a constant fluence of 2.54×10^{13} ions cm^{-2}. This corresponds to a total of 5, 10, and 20 ions striking the lattice within the specified beam diameter respectively. Owing to the consistency in the trends observed for the different ions, this study is carried out for only one case corresponding to an incident Xe ion with energy of 5 keV.

The representative defective lattice obtained from the bombardment of Xe 5 keV ions at fluence of 2.54×10^{13} ions cm^{-2} from a beam diameter of 50 Å [Fig. 14(a)] and 100 Å [Fig. 14(b)]. The characteristics of the defective region with variation of the beam diameter is plotted in Fig. 15. The variation in the number of defects and diameter is such that a (nearly) constant value for the area density (ρ_{area}) is achieved, which is consistent since all the cases corresponds to a constant fluence. However, the height of the defective region is observed to increase for the larger beam diameter cases as a result of more ions striking the lattice. This in turn causes the volume density to decrease with increasing beam diameter.

Although the area density remains almost constant, and the volume density only shows a marginal reduction, the thermal conductivity is found to significantly decrease with the beam diameter. This can be attributed to the much larger size of the defective region when the beam diameter is increased. This suggests that the influence of defective region diameter on the thermal conductivity is more pronounced than the volume

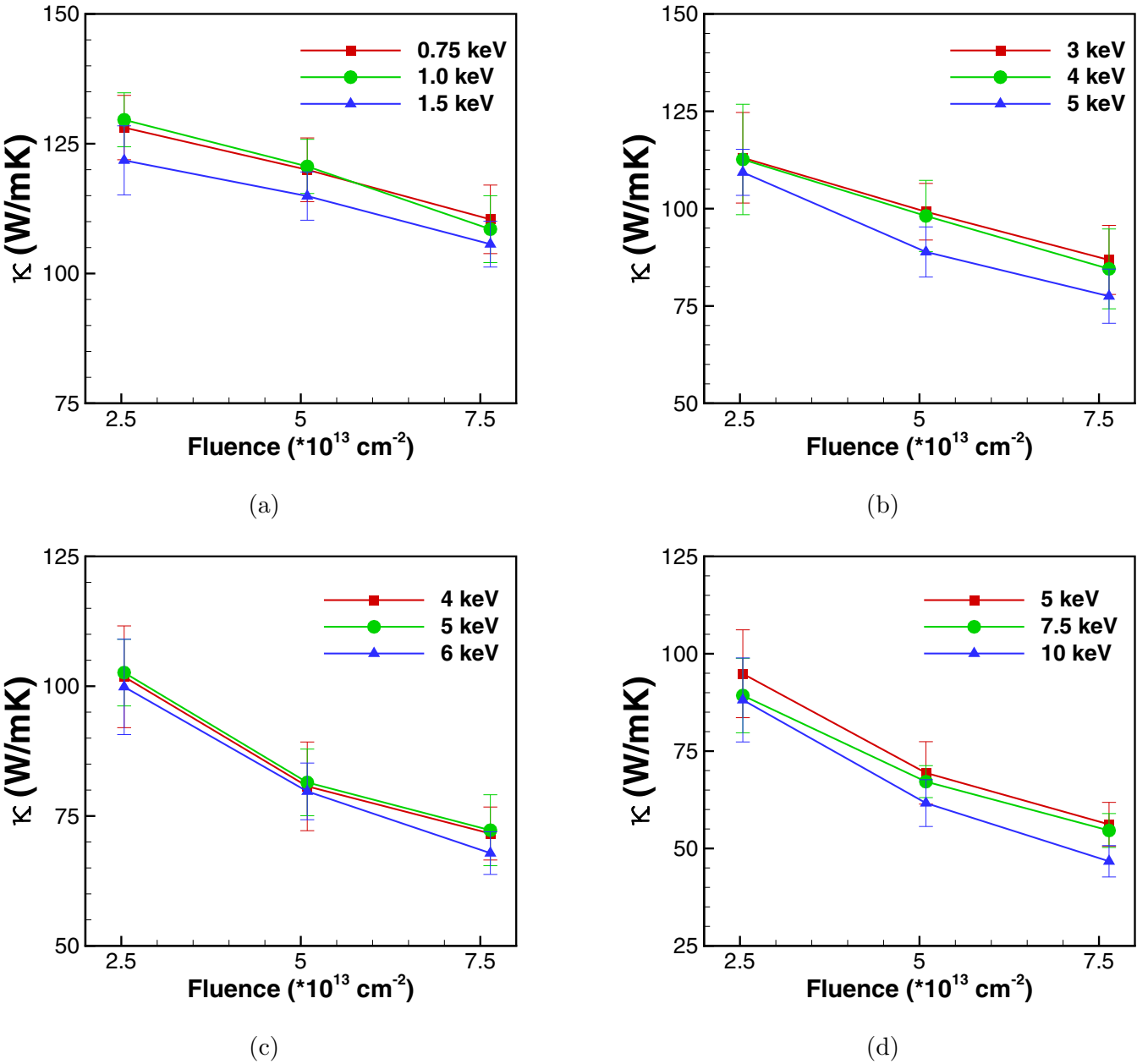

FIG. 13. Thermal conductivity values for representative defective lattice obtained from continuous irradiation of silicon at multiple fluences with (a) Ne(10), (b) Ga(31), (c) Xe(54), and (d) Pt(78) ions of different energies.

density. Also, it is observed that the variation in diameter of the defective region with the beam diameter is much more pronounced than in the previous cases with varying energy and ion atomic number. Hence the beam diameter is an important factor influencing the defective region diameter.

Figure 16 shows the DRDF and the DDDF for the three different beam diameters. The shape of the DRDF widens with the higher beam diameters. The marginal decrease in the magnitude of the peak is attributed to the increasing height of the defective region with the beam diameter. The DDDF plots for the different cases are very similar, having the same magnitude for both the peaks, but with a shift in the position. This shift is also a consequence of the increasing height, due to more ions bombarding the lattice at higher beam diameters.

VI. CONCLUSION

In this study, the structural and thermal effects of the defect configurations produced at the atomic level during continuous energetic ion bombardment in 3D silicon is characterized. Molecular dynamics (MD) simulations closely resembling a tight ion beam processing setup were carried out at room temperatures taking into account the effect of annealing and electronic stopping. The effect of a number of experimental design parameters including the ion species (atomic number), energy, fluence and beam width on the defect configurations and the thermal conductivity of the lattice were investigated. Since the different properties of the material may depend upon various characteristics of the defect configuration, a broad range of the defect characteristics are presented in this study.

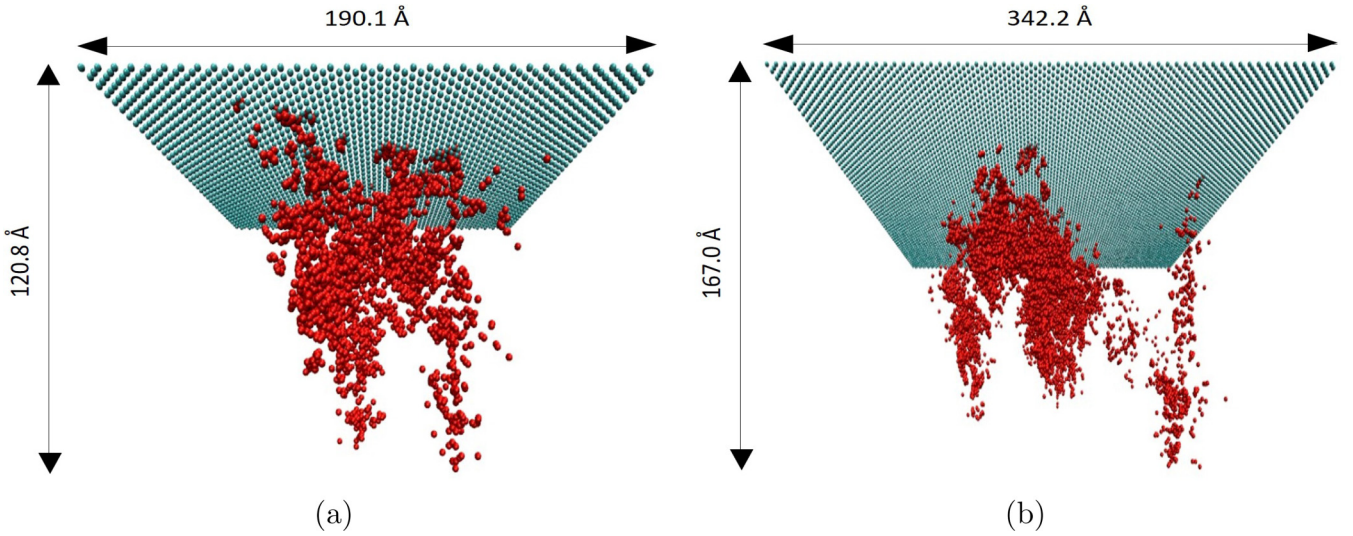

FIG. 14. Perspective view of a representative defective silicon lattice produced by irradiation of Xe(54) 5-keV ions at a constant fluence of 2.54×10^{13} ions cm^{-2} for a beam diameter of (a) $d = 50$ and (b) 100 Å . The pristine regions are transparent, while the defective and surface atoms are indicated by red and cyan respectively.

The number of vacancies and interstitials is quantified using the criteria of half the nearest-neighbor radius spheres. In order to characterize the size of the defective region, it is cast as a cylindrical region. The diameter and height of the defective region is used to compute the area density (ρ_{area}) and volume density (ρ_{vol}). In addition, the radial (DRDF) and depth (DDDF) distribution of the defects within this defective region is also characterized. Further, the amorphous pockets

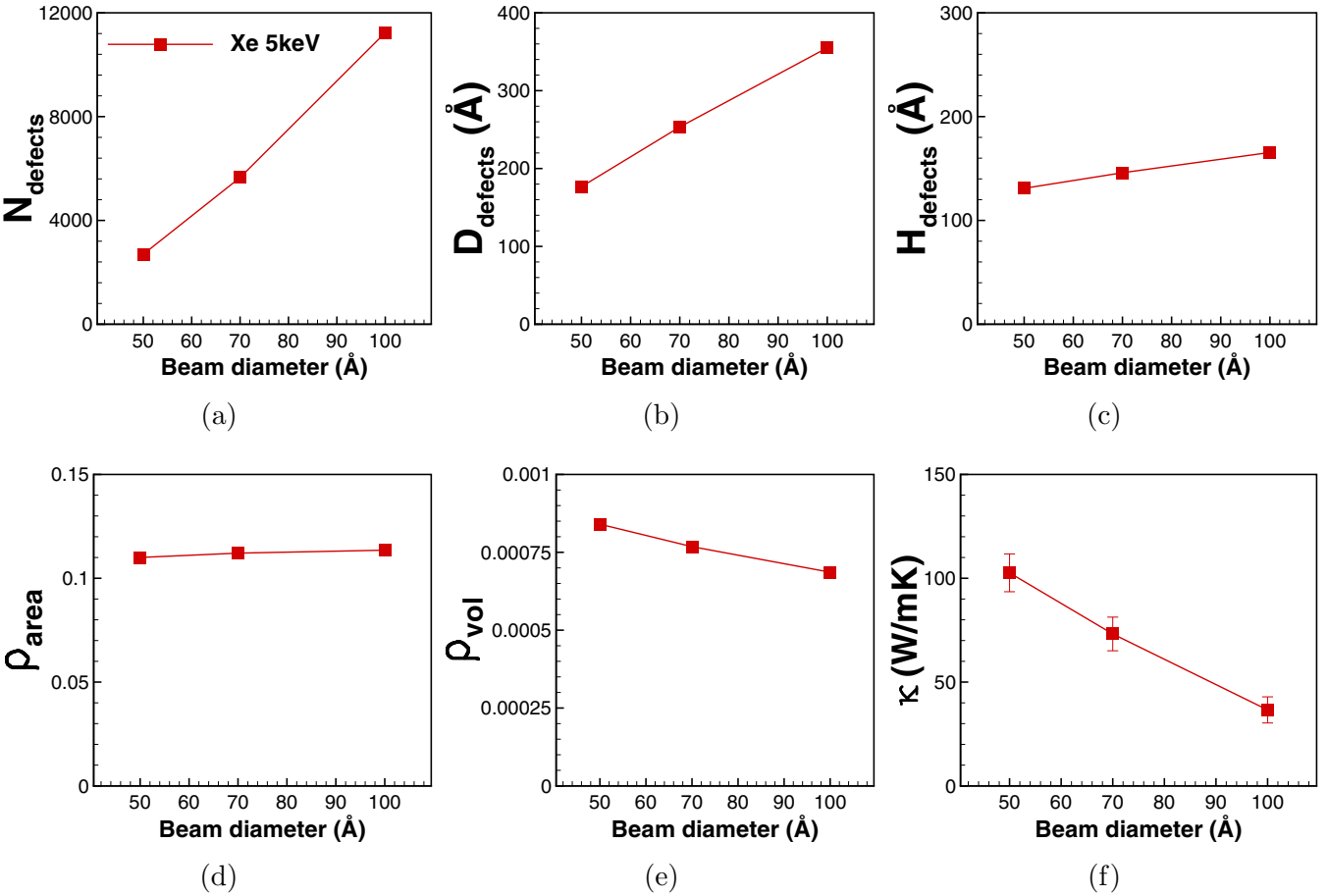

FIG. 15. (a) Average number of defects, (b) diameter, (c) height, (d) area density, (e) volumetric density, and (f) thermal conductivity of the defective region for irradiation of silicon with Xe(54) 5-keV ions at a fluence of 2.54×10^{13} ions cm^{-2} and varying beam diameters.

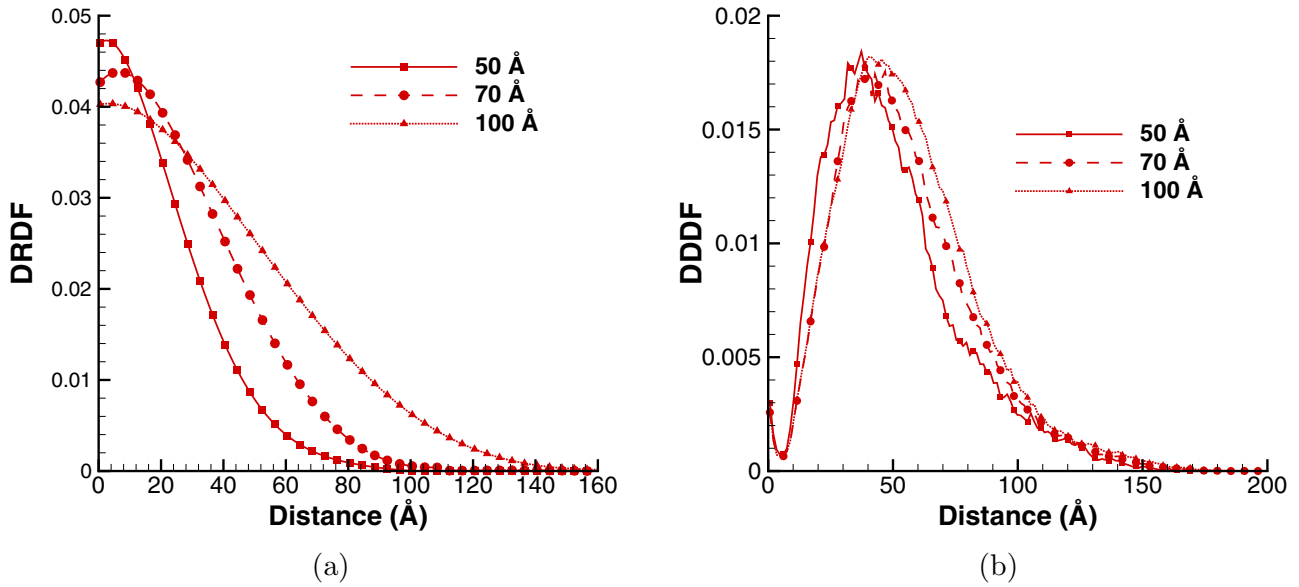

FIG. 16. (a) Defect radial distribution function (DRDF) and (b) defect depth distribution function (DDDF) for irradiation of silicon with Xe(54) 5-keV ions at a fluence of 2.54×10^{13} ions cm^{-2} and varying beam diameters.

produced during ion irradiation are analyzed by characterizing them as defect clusters and computing their properties. Finally, the thermal conductivity is also calculated for each of the cases by choosing a representative lattice, most closely matching the average properties.

It was also demonstrated that the results of the single ion irradiation simulations cannot be directly extrapolated to predict the properties of the defective regions produced under continuous bombardment of the lattice by multiple ions. Hence multi-ion impact simulations are necessary for understanding the defect formation characteristics, trends, and consistent comparison with experiments.

The number of defects, diameter, and height of the defective region were observed to monotonically increase with the energy of the ion. However, the rate of increase of each were quite different for each of the quantities. The area density and volume density are found to exhibit opposite trends, where the ρ_{area} is found to increase with energy, while the ρ_{vol} decreases. Hence the energy of the ion can be a useful parameter to achieve desired material properties, which are uniquely influenced by the area and volumetric densities. The increasing diameter and decreasing volumetric density were observed to have opposing effects on the thermal conductivity leading to negligible variation in the thermal conductivity and no clear trends could be discerned owing to the error bars associated with the Green-Kubo methodology.

At a fixed energy and fluence, increasing the ion atomic number is found to increase the number of defects, but leads to a defective region of smaller height and diameter, which is attributed to the greater interaction potential of the larger ions. Consequently, the area and the volume density increases with the ion atomic number. The ion atomic number is found to be the most influential parameter for controlling the density of the defects within a region. Thus regions of high defect densities can be produced by larger ions with smaller energies. All of the defect characteristics were observed to continually increase with the fluence, while the thermal conductivity was found to monotonically decrease. Reasonable estimation for the number of defects and other properties of the defective region can be obtained for other ions, (reasonable) energy and fluence ranges from the results presented in this study.

The DRDF profiles for all the cases were found to uniformly decrease with the radial distance. Both the ion atomic number and fluence lead to a larger peak and a greater spread in the DRDF, and these effects are more pronounced than the energy of the ion (in the energy ranges considered). The DDDF is characterized by two peaks, a smaller one at the surface and a larger peak within the lattice. Increasing ion energies leads to a wider DDDF distribution and a lower internal peak which is shifted further away from the surface. The ion atomic number has the exact opposite trend and results in a more narrow distribution with a higher second peak, that is closer to the surface. On the other hand, larger fluences cause the DDDF profile to broaden and also lead to a peak with greater magnitude that is marginally shifted further into the lattice. These detailed distributions (DRDF and DDDF) provide reasonably accurate (representative) defective regions, which can be directly used to investigate the change in various physical properties of the system due to irradiation.

Analyzing the properties of the defect clusters showed that most of defects occurred in large clusters, with very few isolated defects, resulting from the short RCS in semiconductors. In addition, the isolated single defects were found to be almost twice that of isolated Frenkel defects, suggesting that RCS is long enough to displace the atoms from its original position by a distance greater than one bond length. Due to the higher penetration of the lower mass ions, the fraction of isolated defects is found to decrease with the ion atomic number. The energy of the ion has little influence on the cluster size and fraction of isolated defects, suggesting that the cascade dynamics and defect formation does not vary substantially with energy (in the ranges considered). The average cluster

size is observed to increase with the fluence, which is attributed to two reasons, the greater overlap of the cascade regions of multiple ions, and the lower stability of the defective regions, making it more susceptible to further damage.

Finally, the effect of varying the beam diameter at a fixed fluence was examined. Although the area density remained constant, the height of the defective region exhibited a slight increase with beam diameter, leading to decrease in the volume density of the defects. The rate of increase of the defective region diameter was found to be more pronounced in comparison with the previous parameters of energy, atomic number and fluence, which implies that the beam diameter is the major factor in determining the diameter of the defective region. This is of great significance from an experimental view point since the beam diameter is an easily controllable design parameter. Wider DRDF profiles with marginally decreasing peaks were observed with increasing beam diameter. The DDDF profiles for the different cases were qualitatively and quantitatively similar, with peaks of same magnitude, which were shifted slightly away from the surface with increasing beam diameter. Although only marginal variation was observed in the defect densities, a sharp decrease in the thermal conductivity is found with increasing beam diameter resulting from the larger size of the defective region. This suggests that the size of the defective region has a greater influence in modifying the thermal conductivity in comparison with the defect density. This study indicates that ion beam irradiation can be a realizable manufacturing process with high tunability and control. The data presented in this work can be utilized to inform and select the suitable irradiation parameters to introduce specific types of defects in a silicon target for tailoring the desired material properties.

ACKNOWLEDGMENTS

This work is supported by the National Science Foundation through Grant No. EAGER-1550895.

[1] J. W. Mayer and S. S. Lau, *Electronic Materials Science: For Integrated Circuits in Si and GaAs* (Prentice Hall, New York, 1990).

[2] G. J. Snyder and E. S. Toberer, Complex thermoelectric materials, Nat. Mater. **7**, 105 (2008).

[3] C. Bhandari and D. M. Rowe, *Crc Handbook of Thermoelectrics* (Chemical Rubber Corporation, Boca Raton, 1955), p. 55.

[4] A. X. Levander, T. Tong, K. M. Yu, J. Suh, D. Fu, R. Zhang, H. Lu, W. J. Schaff, O. Dubon, W. Walukiewicz, D. G. Cahill, and J. Wu, Effects of point defects on thermal and thermoelectric properties of InN, Appl. Phys. Lett. **98**, 012108 (2011).

[5] F. Banhart and P. Ajayan, Carbon onions as nanoscopic pressure cells for diamond formation, Nature (London) **382**, 433 (1996).

[6] A. Hashimoto, K. Suenaga, A. Gloter, K. Urita, and S. Iijima, Direct evidence for atomic defects in graphene layers, Nature (London) **430**, 870 (2004).

[7] B. Peng, M. Locascio, P. Zapol, S. Li, S. L. Mielke, G. C. Schatz, and H. D. Espinosa, Measurements of near-ultimate strength for multiwalled carbon nanotubes and irradiation-induced crosslinking improvements, Nat. Nanotechnol. **3**, 626 (2008).

[8] A. V. Krasheninnikov and K. Nordlund, Ion and electron irradiation-induced effects in nanostructured materials, J. Appl. Phys. **107**, 071301 (2010).

[9] M.-J. Caturla, T. Díaz de la Rubia, L. A. Marqués, and G. H. Gilmer, Ion-beam processing of silicon at keV energies: A molecular-dynamics study, Phys. Rev. B **54**, 16683 (1996).

[10] K. Nordlund and R. S. Averback, Point defect movement and annealing in collision cascades, Phys. Rev. B **56**, 2421 (1997).

[11] K. Nordlund, M. Ghaly, R. S. Averback, M. Caturla, T. Diaz de la Rubia, and J. Tarus, Defect production in collision cascades in elemental semiconductors and fcc metals, Phys. Rev. B **57**, 7556 (1998).

[12] O. Lehtinen, E. Dumur, J. Kotakoski, A. Krasheninnikov, K. Nordlund, and J. Keinonen, Production of defects in hexagonal boron nitride monolayer under ion irradiation, Nucl. Instrum. Methods Phys. Res., Sect. B **269**, 1327 (2011).

[13] O. Lehtinen, B. Naydenov, P. Börner, K. Melentjevic, C. Müller, L. P. McGuinness, S. Pezzagna, J. Meijer, U. Kaiser, and F. Jelezko, Molecular dynamics simulations of shallow nitrogen and silicon implantation into diamond, Phys. Rev. B **93**, 035202 (2016).

[14] K. A. Stephani and I. D. Boyd, Molecular dynamics modeling of defect formation in many-layer hexagonal boron nitride, Nucl. Instrum. Methods Phys. Res., Sect. B **365**, 235 (2015).

[15] E. P. Bellido and J. M. Seminario, Molecular dynamics simulations of ion-bombarded graphene, J. Phys. Chem. C **116**, 4044 (2012).

[16] T. Zhu, K. Swaminathan-Gopalan, E. Ertekin, and K. A. Stephani, Silicon metamaterials patterned by ion beam irradiation for thermoelectric applications (unpublished).

[17] J. A. Anderson, C. D. Lorenz, and A. Travesset, General purpose molecular dynamics simulations fully implemented on graphics processing units, J. Comput. Phys. **227**, 5342 (2008).

[18] J. F. Ziegler, J. Biersack, and U. Littmark, *The Stopping and Range of Ions in Matter* (Pergamon, New York, 1985), Vol. 1.

[19] J. Tersoff, Empirical interatomic potential for silicon with improved elastic properties, Phys. Rev. B **38**, 9902 (1988).

[20] J. F. Ziegler, M. Ziegler, and J. Biersack, SRIM The stopping and range of ions in matter (2010), Nucl. Instrum. Methods Phys. Res., Sect. B **268**, 1818 (2010).

[21] K. Nordlund, Molecular dynamics simulation of ion ranges in the 1-100 keV energy range, Comput. Mater. Sci. **3**, 448 (1995).

[22] P. Echenique, F. Flores, and R. Ritchie, Dynamic screening of ions in condensed matter, Solid State Phys. **43**, 229 (1990).

[23] O. Lehtinen, J. Kotakoski, A. V. Krasheninnikov, A. Tolvanen, K. Nordlund, and J. Keinonen, Effects of ion bombardment on a two-dimensional target: Atomistic simulations of graphene irradiation, Phys. Rev. B **81**, 153401 (2010).

[24] J. Tersoff, New empirical approach for the structure and energy of covalent systems, Phys. Rev. B **37**, 6991 (1988).

[25] R. Devanathan, T. D. de la Rubia, and W. Weber, Displacement threshold energies in β-sic, J. Nucl. Mater. **253**, 47 (1998).

[26] H. J. C. Berendsen, J. P. M. Postma, W. F. van Gunsteren, A. DiNola, and J. R. Haak, Molecular dynamics with coupling to an external bath, J. Chem. Phys. **81**, 3684 (1984).

[27] M. P. Allen and D. J. Tildesley, *Computer Simulation of Liquids* (Clarendon Press, Oxford, 1989).

[28] R. Averback, T. Diaz de la Rubia, H. Ehrenfest, and F. Spaepen, *Solid State Physics*, Vol. 51 (Academic, New York, 1997), pp. 281–402.

[29] T. D. De La Rubia, R. Averback, R. Benedek, and W. King, Role of Thermal Spikes in Energetic Displacement Cascades, Phys. Rev. Lett. **60**, 76 (1988).

[30] M. S. Green and M. R. Processes, Markoff random processes and the statistical mechanics of time-dependent phenomena. II. Irreversible processes in fluids, J. Chem. Phys. **22**, 398 (1954).

[31] R. Kubo, Statistical-mechanical theory of irreversible processes. I. General theory and simple applications to magnetic and conduction problems, J. Phys. Soc. Jpn. **12**, 570 (1957).

[32] S. G. Volz and G. Chen, Molecular-dynamics simulation of thermal conductivity of silicon crystals, Phys. Rev. B **61**, 2651 (2000).

[33] P. K. Schelling, S. R. Phillpot, and P. Keblinski, Comparison of atomic-level simulation methods for computing thermal conductivity, Phys. Rev. B **65**, 144306 (2002).

[34] J. Chen, G. Zhang, and B. Li, How to improve the accuracy of equilibrium molecular dynamics for computation of thermal conductivity? Phys. Lett. A **374**, 2392 (2010).

[35] W. Fulkerson, J. P. Moore, R. K. Williams, R. S. Graves, and D. L. McElroy, Thermal conductivity, electrical resistivity, and seebeck coefficient of silicon from 100 to 1300 K, Phys. Rev. **167**, 765 (1968).

[36] J. Lee, J. Grossman, J. Reed, and G. Galli, Lattice thermal conductivity of nanoporous Si: Molecular dynamics study, Appl. Phys. Lett. **91**, 223110 (2007).

[37] L. J. Porter, S. Yip, M. Yamaguchi, H. Kaburaki, and M. Tang, Empirical bond-order potential description of thermodynamic properties of crystalline silicon, J. Appl. Phys. **81**, 96 (1997).

[38] L. Howe and M. Rainville, Features of collision cascades in silicon as determined by transmission electron microscopy, Nucl. Instrum. Methods **182**, 143 (1981).

[39] Y. Zhu, Z. X. Cai, R. C. Budhani, M. Suenaga, and D. O. Welch, Structures and effects of radiation damage in cuprate superconductors irradiated with several-hundred-mev heavy ions, Phys. Rev. B **48**, 6436 (1993).

[40] D. Kiener, P. Hosemann, S. Maloy, and A. Minor, *In situ* nanocompression testing of irradiated copper, Nat. Mater. **10**, 608 (2011).

[41] J. Spitznagel, S. Wood, W. Choyke, N. Doyle, J. Bradshaw, and S. Fishman, Ion beam modification of 6H/15R SiC crystals, Nucl. Instrum. Methods Phys. Res., Sect. B **16**, 237 (1986).

[42] M. C. Moore, N. Kalyanasundaram, J. B. Freund, and H. T. Johnson, Structural and sputtering effects of medium energy ion bombardment of silicon, Nucl. Instrum. Methods Phys. Res., Sect. B **225**, 241 (2004).

[43] C. D. Hardie, C. A. Williams, S. Xu, and S. G. Roberts, Effects of irradiation temperature and dose rate on the mechanical properties of self-ion implanted Fe and Fe–Cr alloys, J. Nucl. Mater. **439**, 33 (2013).

[44] J.-P. Salvetat, J.-M. Bonard, N. Thomson, A. Kulik, L. Forro, W. Benoit, and L. Zuppiroli, Mechanical properties of carbon nanotubes, Appl. Phys. A **69**, 255 (1999).

[45] E. Ertekin, D. C. Chrzan, and M. S. Daw, Topological description of the stone-wales defect formation energy in carbon nanotubes and graphene, Phys. Rev. B **79**, 155421 (2009).

[46] S. Okada, Atomic configurations and energetics of vacancies in hexagonal boron nitride: First-principles total-energy calculations, Phys. Rev. B **80**, 161404 (2009).

[47] S. Azevedo, J. Kaschny, C. De Castilho, and F. de Brito Mota, Electronic structure of defects in a boron nitride monolayer, Eur. Phys. J. B **67**, 507 (2009).

[48] Q. Wang, Q. Sun, G. Chen, Y. Kawazoe, and P. Jena, Vacancy-induced magnetism in ZnO thin films and nanowires, Phys. Rev. B **77**, 205411 (2008).

[49] Y. Zhang, S. Talapatra, S. Kar, R. Vajtai, S. Nayak, and P. M. Ajayan, First-Principles Study of Defect-Induced Magnetism in Carbon, Phys. Rev. Lett. **99**, 107201 (2007).

[50] M. Sayed, J. Jefferson, A. Walker, and A. Cullis, Computer simulation of atomic displacements in Si, GaAs, and AlAs, Nucl. Instrum. Methods Phys. Res., Sect. B **102**, 232 (1995).

[51] M. Caturla, T. de la Rubia, G. Gilmer, and R. Culbertson, Materials synthesis and processing using ion beams, in *MRS Symposia Proceedings*, Vol. 316 (MRS, Boston, 1994), p. 111.